# Beyond the First Quadrant: Origin of the High Frequency Intensity-Modulated Photocurrent/Photovoltage Spectroscopy Response of Perovskite Solar Cells

*Adam Pockett,\* Michael Spence, Suzanne K. Thomas, Dimitrios Raptis, Trystan Watson, and Matthew J. Carnie\**

The complete interpretation of small perturbation frequency-domain measurements on perovskite solar cells has proven to be challenging. This is particularly true in the case of intensity-modulated photocurrent/photovoltage spectroscopy (IMPS/IMVS) measurements in which the high frequency response is obscured by instrument limitations. Herein, a new experimental methodology capable of accurately resolving the high frequency response—often observable in the second and third quadrants of the complex plane—of a range of perovskite devices is demonstrated. By combining single-frequency IMPS/IMVS measurements, it is able to construct the time dependence of the IMPS/IMVS response of these devices during their initial response to illumination. This reveals significant negative photocurrent/photovoltage signals at high frequency while devices reach steady state, which is in keeping with observations made from comparable time-domain transient measurements. These techniques allow the underlying interfacial recombination and ion migration processes to be assessed, which are not always evident using steady-state measurements. The ability to study and mitigate these processes is vital in optimizing the real-world operation of devices.

## 1. Introduction

Despite the impressive rise in performance of perovskite solar cells, the operation of devices is still not fully understood. A range of properties have been well defined, such as the importance of the passivation of surfaces and interfaces, which has led to substantial improvements in open-circuit voltage.[1–3] However, it is likely that to optimize all device parameters, and perhaps more importantly to ensure that this optimization

Dr. A. Pockett, M. Spence, Dr. S. K. Thomas, Dr. D. Raptis,
Prof. T. Watson, Dr. M. J. Carnie
Materials Research Centre
College of Engineering
SPECIFIC – Swansea University
Bay Campus, Swansea SA1 8EN, UK
E-mail: adam.pockett@swansea.ac.uk; m.j.carnie@swansea.ac.uk

The ORCID identification number(s) for the author(s) of this article can be found under https://doi.org/10.1002/solr.202100159.

in absolute efficiency translates to variable, real-world conditions, that a more complete understanding is achieved. An area of particular complexity is the interaction of electronic and ionic charges within the perovskite. This has been shown to give rise to a range of interesting phenomena in the behavior of devices in response to light and/or voltage stimuli—such as current–voltage ($J$–$V$) hysteresis,[4–6] and an exceptionally slow rise in the open-circuit voltage under illumination for some devices.[7–9]

Optoelectronic characterization techniques such as transient photovoltage/photocurrent (TPV/TPC)[6,7,10–12] and impedance spectroscopy (IS)[13–16] have been used extensively to study the link between electronic and ionic properties of perovskite devices. In general, these studies show evidence of multiple processes occurring on distinct timescales—i.e., a high frequency/short time response occurring on the megahertz/microsecond timescale, and a low frequency response occurring on the hertz/second timescale. These processes can be broadly categorized as being the fast electronic response and slow ionic response of the device. However, it is clear there is a link between these two processes. Numerous studies have shown that the ionic distribution within the active layer affects the rate of recombination, particular at the interfaces with contact layers.[17–19] In particular, it has been shown that the presence of interfacial recombination results in a negative spike in response to the laser pulse in TPV measurements.[6,7,11,20] A similar negative spike has been observed in TPC measurements, which is also related to the ionic distribution near the interfaces—leading to the formation of electric potential valleys, causing the initial photocurrent to have an opposite direction to standard operation.[6,12] These negative responses diminish as the ionic charges diffuse away from the interfaces during light soaking.

This complex behavior has made it difficult to determine a reliable equivalent circuit for obtaining useful device parameters from IS measurements.[21–23] A complimentary technique, intensity-modulated photocurrent spectroscopy (IMPS), has been used in conjunction with IS in an attempt to improve this understanding.[15,24–27] IMPS measures the frequency-dependent photocurrent response to a sinusoidally modulated incident light

stimulus, with the cell held at a fixed potential (usually short-circuit). The analogous technique, intensity-modulated photo-voltage spectroscopy (IMVS), has also been used to measure the photovoltage response at open-circuit. Similarly to the IS response, IMPS/IMVS measurements reveal multiple processes occurring over a wide frequency range—resulting in multiple arcs and loops when presented on a typical Nyquist plot.[25,26,28]

Much of the focus of these studies has been on the lower frequency range in which these additional arcs and loops usually manifest. The high frequency IMPS is limited by the RC time constant of the device (time constant of charging the device geometric capacitance through the series resistance), and so does not usually reveal useful information about recombination and/or transport within the device.[29] In addition, it is challenging to accurately resolve the high frequency response above ≈100 kHz due to instrument limitations. At such high frequencies, the attenuation and phase lag induced between the driving current and light-emitting diode (LED) output is significant, resulting in low signal-to-noise ratios and unusual phase shifts in the measured current response.[13,15,25,30] Due to the frequency limitation of many commercial systems, the high frequency response is usually not fully resolved, but often appears to cross into the second quadrant of the Nyquist plot.[13,25,30] The high frequency behavior has therefore been largely overlooked in previous literature reports, with many studies ascribing the atypical response purely to instrumental limitations. Almora et al. have observed negative phase shifts at high frequency in IMPS and IMVS measurements which led to negative inductive loops in light intensity-modulated derived impedance spectra—while not studied in detail, it was postulated that these features can possibly be linked to interfacial recombination.[30]

In this article, we show that through the careful design of the measurement hardware the high frequency IMPS/IMVS response can be accurately resolved. This reveals the presence of additional processes at high frequency, which evolve over time under initial illumination, that have not previously been observed in these measurements. By combining these measurements with their equivalent time-domain techniques, TPV and TPC, we associate these time-dependent negative phase shifts to the presence of significant interfacial recombination and ionic redistribution within the devices during the light-soaking process.

## 2. Results and Discussion

To overcome the usual limit of high frequency modulation of commercial LED-based systems, we have designed a custom-built system which uses separate LEDs for the DC and AC illumination components. By using a small LED for the AC modulation, the required amplitude of the driving signal is reduced, which allows for higher frequency modulation with reduced attenuation and phase shift. We also carefully correct for residual attenuation and phase shift, which allows us to accurately resolve the IMPS and IMVS response at frequencies up to 4 MHz (full experimental considerations are given in the Experimental Section). Figure S7, Supporting Information, shows typical IMPS and IMVS measurements of a triple-mesoporous carbon-based perovskite device (meso-C) at steady state, performed using a commercial system and the system built for this

study. The commercial system has a specified maximum frequency of 200 kHz (although it is possible to measure at higher frequencies). Despite a feedback system controlling the intensity modulation, there is a significant and unusual phase shift for frequencies above 100 kHz. For IMPS, this appears to form a loop through the second and third quadrants, approaching the origin at 1 MHz. The phase shift for the IMVS response causes the high frequency response to dip into the fourth quadrant—again a highly unusual response. As these measurements extend beyond the specification of the system, the reliability of these high frequency responses is questionable. For comparison, the IMPS and IMVS measurements performed using our custom system appear to be more typical—there is a single high frequency arc which approaches the origin, while crossing into the second quadrant marginally. It should be noted that IMPS Nyquist plots are presented here with units of "photocurrent" —an alternate representation with dimensionless transfer function, "Q," related to the external quantum efficiency,[24,31] is shown in Figure S6, Supporting Information, for each device type measured at steady state.

In addition, although these measurements are usually performed with the device at steady-state conditions, the slow dynamic response of many perovskite devices allows us to consider the changing frequency response over time. This was achieved by measuring the modulated photocurrent/voltage response at individual frequencies over time after illumination, whereas the device is acclimating to a steady state. In essence, this approach is comparable to time domain transient measurements in which repeated TPV measurements are taken during the slow $V_{oc}$ rise.[11] Between each frequency condition, the device is left in the dark for long enough for an equilibrium condition to be reached (see the Supporting Information for a schematic illustrating the measurement procedure and an example of the recorded data). By taking the measurements for each frequency, at each particular time after illumination starts, we can construct Nyquist plots giving the IMPS/IMVS response over time. Measurements were performed over the frequency range 4 MHz to 10 Hz, with data recorded at 0.5 s intervals. The lower frequency limit is chosen as it is not practical or relevant to measure the change in a lower frequency process at such short intervals.

As we have previously reported, meso-C devices show an exceptionally slow response to illumination.[7] We therefore focused much of our attention on these devices and measured both the IMPS and IMVS response over time under illumination as the short-circuit current ($J_{sc}$) or open-circuit voltage ($V_{oc}$) was rising to a steady state (see the Experimental Section and Supporting Information for more details). The IMPS response immediately after illumination is shown in **Figure 1** (IMVS response is shown in Figure S8, Supporting Information). Strikingly, at high frequency, we initially observe large arcs crossing into the third and second quadrants of the Nyquist plot for both measurements. This negative response indicates a switching of the sign of the photocurrent/photovoltage response at high frequency—consistent with the negative photocurrent/photovoltage responses observed in equivalent time-domain transient measurements upon laser pulse excitation.[6,11] For IMPS, the time constant of the high frequency arc observed in the third quadrant is $\tau_{IMPS,\ t=0\,min} = 212$ ns. This agrees well with the RC time constant calculated from the product of the series
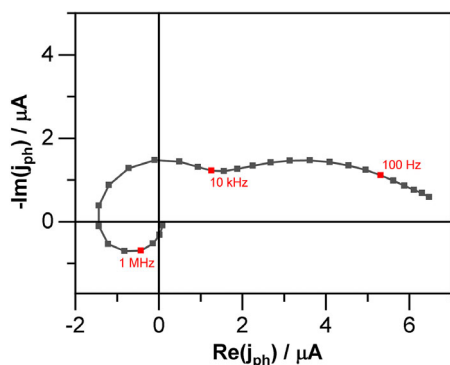
**Figure 1.** IMPS response of meso-C cell immediately after the illumination is turned on.

resistance and geometric capacitance extracted from IS measurements on the same device under steady state conditions—$\tau_{IS} = 248$ ns (see Figure S9, Supporting Information). This is a further indication that this IMPS measurement represents a true device response and is not a consequence of instrumentation limitations. The origin of the mid frequency arc crossing through the second quadrant is less clear, although is consistent with transient measurements—for longer laser pulses, the transient response returns to a positive value after the initial fast negative response.[11] The lower frequency arc represents a process occurring on a longer timescale than usually probed by transient measurements—this frequency range has been studied extensively by others using IMPS.[15,25]

Under continued background illumination, the magnitude of the negative arc decreases, as shown in **Figure 2**a—again suggesting consistency with transient measurements. For comparison, we show the progression of the TPC response at the same time intervals in Figure 2b. From both of these measurements, it can be seen that the negative signal is initially large, and diminishes significantly over the first 2 min of illumination. The photocurrent response becomes purely positive—the IMPS response no longer crosses the real axis at negative values and there is a larger arc into the first quadrant, again consistent with the increase in the positive photocurrent amplitude in transient measurements over time. After extended periods of illumination,

the high frequency IMPS response still loops through the second quadrant, which can be related to the photocurrent rise time.[32] Interestingly, after being illuminated for several minutes, so that the device nears a steady-state condition, the RC time constant extracted from the high frequency arc (now in the first quadrant) no longer agrees with that determined from IS measurements—it increases to $\tau_{IMPS,\ t=5\ min} = 1.35$ µs. The reason for this difference is unclear; however, a similar discrepancy has also been reported in work by Ravishankar et al. which suggested that an additional series resistance effect, due to an as yet unidentified resistive element, being required in the cells equivalent circuit.[15] Alternatively, the modeling by Moia et al. shows a complex equivalent circuit containing a frequency-dependent geometric capacitance, and contact capacitances due to the presence of mobile ions, which may result in a different effective total capacitance, thus altering the RC time constant at steady state.[23] Further consideration of this effect is beyond the scope of this work, but this behavior highlights an interesting phenomenon for future investigation.

To compare the rate of change in the negative photocurrent processes, **Figure 3** shows the relative magnitudes of these negative signal components from both IMPS and TPC. For IMPS, we take the magnitude of the photocurrent 180° out-of-phase with the modulated light stimulus (i.e., the magnitude of the negative arc crossing the real axis), normalized to the initial value. For TPC, we take the amplitude of the negative inflection point of the transient response, again normalized to the initial value. Excellent agreement can be seen between these two different measurements. This again provides further evidence that we are able to resolve the true IMPS response at high frequency. The IMPS measurements are therefore capable of resolving the effects of ion migration on the electric field in the interfacial regions during the slow adjustment of the cell to steady-state under illumination, in a similar manner to that previously shown for TPC measurements.[6,12] Comparable effects are observed for both IMPS and IMVS measurements indicating that the underlying mechanism impacts both short-circuit and open-circuit operation. This effect seems more dominant at open-circuit, with the rate at which the negative photovoltage response diminishes being slower than for the photocurrent response. Although this interfacial recombination behavior only appears dominant during the rise to steady state, we have previously reported that
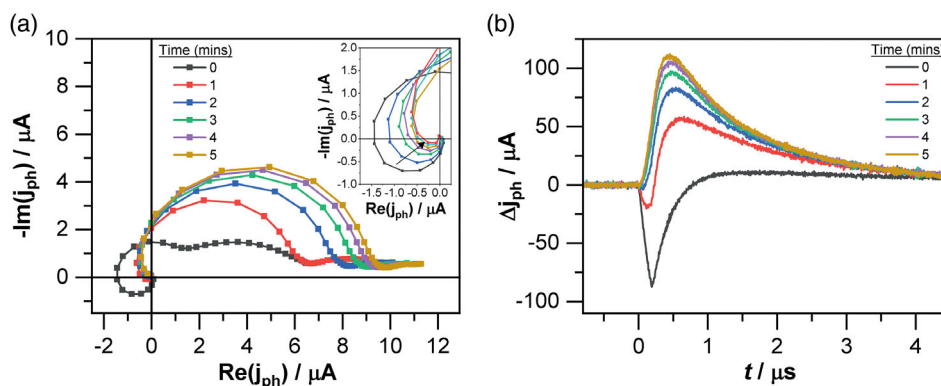


**Figure 2.** a) Progression of IMPS response of meso-C device at 1 min intervals (inset: 10 s intervals for first 1 min after illumination). b) Progression of TPC response at 1 min intervals.
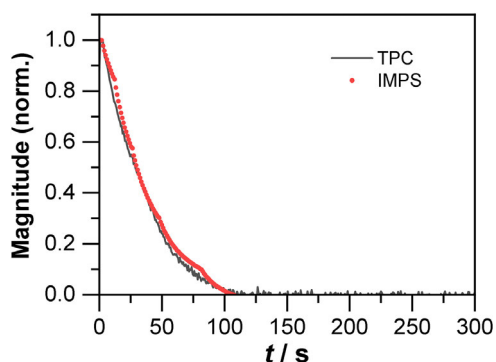
**Figure 3.** Comparison of the relative magnitude of the negative photocurrent signal from IMPS and TPC measurements for a meso-C device.

for some devices it appears to never completely dissipate.[7,11] This shows that the ability to study this type of process is important for optimizing the steady-state operation of devices. In addition, in real-world operation, the device must respond to constantly varying conditions. The underlying impact of these additional recombination processes may reduce performance or response time in these circumstances.

We further highlight the use of these time-dependent IMPS/IMVS techniques by studying the behavior of different device types. To show that the technique is able to accurately determine the high frequency photocurrent and photovoltage response in

devices with fast response times, we also studied inverted architecture nickel oxide ($NiO_x$) contact devices. These devices typically stabilize to a steady state within a few seconds of illumination (see Figure S5, Supporting Information). We observe no negative features in the IMPS or IMVS response at short times after illumination is turned on, as is true in the equivalent transient techniques (see Figure S10, Supporting Information). The IMPS and TPC responses show no evolution of the photocurrent response over time under illumination. There is a small change in the magnitude of the lower frequency photovoltage response over the first 30 s of illumination—a similar small effect is seen in the TPV response. $NiO_x$ devices show fast response times at both short-circuit and open-circuit and so this behavior seems consistent with an absence of interfacial recombination during the rise to a steady state. Indeed, this is also linked to reduced hysteresis in inverted architecture devices such as these.[6,11,33]

The meso-C and $NiO_x$ devices we tested have significantly different response times to illumination. We also measured tin oxide contact devices ($SnO_2$) which have intermediate response times, and are shown in literature to often have a small, but clear level of hysteresis.[34] The stabilization times for $J_{sc}$ and $V_{oc}$ under illumination for these devices is of the order of tens of seconds (see Figure S5, Supporting Information). Despite a relatively slow stabilization in $J_{sc}$, we observed no negative photocurrent response in either IMPS or TPC measurements as shown in **Figure 4**a. Again, this demonstrates consistency
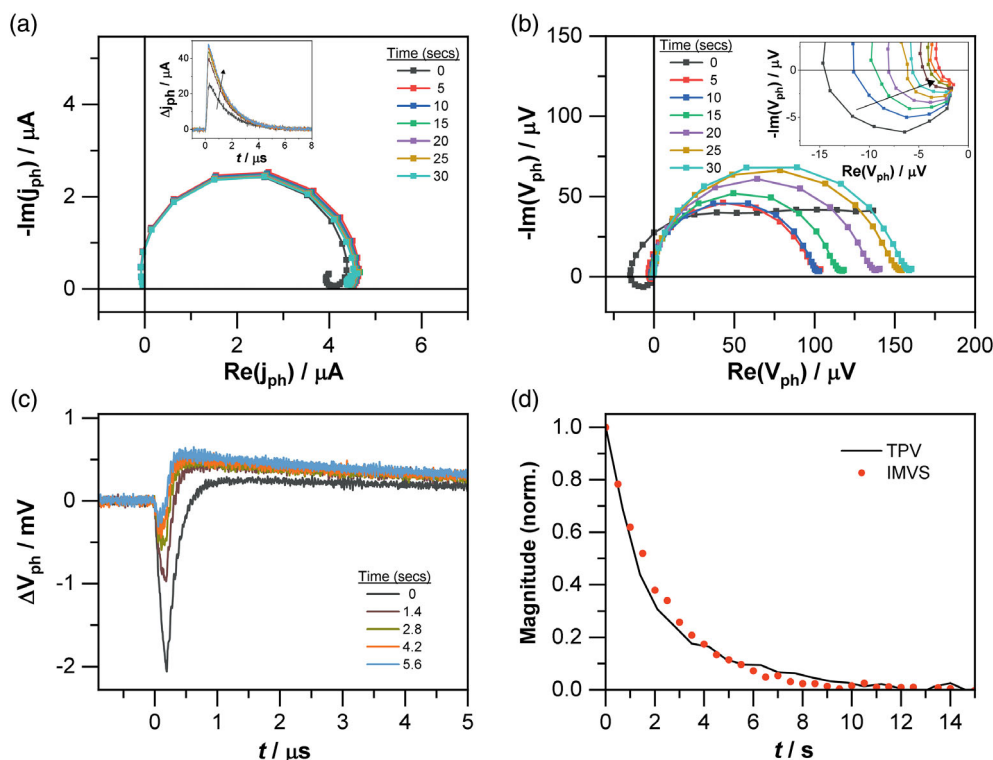


**Figure 4.** a) Progression of IMPS response for $SnO_2$ based cell at 5 s intervals, showing that no negative photocurrent signal is observed (inset: TPC progression for same $SnO_2$ device at 1.4 s intervals, showing that no negative TPC signal is seen even at short times after illumination). b) Progression of IMVS response for $SnO_2$ cell at 5 s intervals (inset: 0.5 s intervals for first 5 s after illumination). c) TPV response at 1.4 s intervals. d) Comparison of the relative magnitude of the negative photovoltage signal from IMVS and TPV measurements of $SnO_2$ device.

between the two techniques, but suggests a different mechanism as being responsible for the slow cell response time compared to the dominance of interfacial ionic effects observed in meso-C devices. We do observe a significant, but short-lived negative photovoltage response in IMVS for $SnO_2$ devices as shown in Figure 4b. The negative arc diminishes over the first 10 s of illumination, and the magnitude of the lower frequency photovoltage response increases. This compares well with the TPV behavior shown in Figure 4c. The negative photovoltage spike quickly disappears, and the amplitude of the positive photovoltage response increases over time. Figure 4d compares the rate at which the negative components of the photovoltage response reduce over time. Excellent agreement can be seen between the two techniques, with the negative components of the two measurements diminishing after $\approx$6 s.

## 3. Conclusion

Through careful design of the experimental hardware, we have shown that the high frequency IMPS/IMVS response of perovskite solar cells contains a number of useful features which can be used to analyze device operation. We have shown that the large phase shifts at high frequency observed in IMPS/IMVS measurements made using many standard instruments are due to instrument limitations. We have been able to demonstrate that the true response at steady state does not contain these large phase shifts, with negative components, in many devices. Interestingly, there are indeed substantial negative photocurrent and photovoltage components under high frequency modulation during the initial stabilization of devices under illumination. By carefully comparing these measurements to equivalent time-domain techniques, it becomes clear that this behavior is linked to the effects of ion migration on the electric field profile and recombination at the device interfaces.

The ability to resolve changes in the frequency response at short timescales allows us to monitor the impact of interfacial recombination and ion migration, even on devices which show relatively fast response times. Although this dynamic behavior may not be detrimental to real-world operation in these devices, as the presence of interfacial recombination appears to be mitigated after a few seconds under illumination due to the rearrangement of the ion distribution, we have shown that it may still act as a significant loss mechanism at steady state for meso-C devices. The ability to carefully characterize this process using these techniques is highly valuable. Analysis of the time dependence of the mid to low frequency response, although beyond the scope of this article, may also provide useful insights into device operation.

## 4. Experimental Section

*Device Preparation*: Mesoporous carbon devices were prepared using a previously described method.[7] Briefly, a compact $TiO_2$ blocking layer was sprayed with a solution of 10% titanium di-isopropoxide bis (acetylacetonate) in IPA on FTO substrates, which were kept at 300 °C on a hot plate. Mesoporous layers of $TiO_2$, $ZrO_2$, and carbon were sequentially screen printed—the annealing of each layer occurred at 550 °C for $TiO_2$, and 400 °C for $ZrO_2$ and carbon. The cooled mesoporous stack was infiltrated with a perovskite solution containing 0.439 g $PbI_2$,

0.1514 g MAI, and 0.0067 g of 5-AVAI in 1 mL γ-butyrolactone. Allowing 10 min time for the solution to percolate throughout the stack, the devices were annealed in a fan oven for 1 h at 50 °C. The finished solar cells were then exposed to 70% relative humidity at 40 °C for 24 h to induce a recrystallization and then dried in a vacuum oven.

For $SnO_2$ devices, tin (IV) oxide nanoparticles (Alfa Aesar, 15% in $H_2O$ colloidal dispersion) were diluted in deionized water in volumetric ratio of 1:3 and spin coated on ITO substrates at 3000 rpm for 30 s, before annealing on a hotplate at 140 °C for 45 min in air. The samples were then transferred to a nitrogen filled glove box for deposition of the perovskite and hole-transporting layer. For the perovskite precursor, lead iodide (TCI Chemicals, 99.99%, trace metals basis) and methylammonium iodide (Greatcell Solar) were dissolved in a 4:1 ratio of N,N-dimethylformamide (Sigma Aldrich, anhydrous 99.8%):dimethyl sulfoxide (Sigma Aldrich, anhydrous ≥99.9%) to give a 1.2 M solution with a 5% lead excess. The $MAPbI_3$ precursor was spin coated at 4000 rpm for 30 s. After 6 s, 200 µL of ethyl acetate was dropped onto the spinning substrate to aid crystallization of the perovskite. The films were then annealed on a hotplate for 10 min at 100 °C. Spiro-OMeTAD (Sigma Aldrich, 99% (HPLC)) was dissolved in chlorobenzene (Sigma Aldrich, anhydrous 99.8%) to make a 73 mM solution, with the following additives: 19 µL mL$^{-1}$ of bis(-trifluoromethane)sulfonimide lithium salt (Sigma Aldrich, 99.95%) (1.8 M stock solution in Acetonitrile (Sigma Aldrich)), 10 µL mL$^{-1}$ FK 209 Co(III) TFSI salt (Sigma Aldrich) (0.2 M in Acetonitrile), and 34 µL mL$^{-1}$ of 4-tert-butylpyridine (4-tBP) (Sigma Aldrich, 98%). Spiro-OMeTAD was dynamically spin coated with the substrate spinning at 4000 rpm and left to spin for a further 10 s and dried at room temperature. Gold contacts were thermally evaporated through a shadow mask.

$NiO_x$ devices were prepared on ITO substrates via a previously described method, using a PCBM/BCP electron transport layer.[35]

*J–V Characterization*: Masked devices (meso-C: 0.5 cm$^2$, $SnO_2/NiO_x$: 0.1 cm$^2$) were tested under a class AAA solar simulator (Newport Oriel Sol3A) at AM1.5 100 mW cm$^{-2}$ illumination conditions (calibrated using a KG5 filtered reference cell) using a Keithley 2400 source meter. The devices were scanned from $V_{oc}$ to $J_{sc}$ and vice versa at a scan rate of 330 mV s$^{-1}$, after 3 min of light soaking.

*Custom-Built High Frequency IMPS/IMVS Setup*: In most cases, commercially available and custom-built IMPS/IMVS measurement systems used a single LED to provide both the DC illumination bias and the superimposed AC modulation. This required a large, high current LED to provide a significant DC illumination offset. The modulated driving current required was therefore also relatively large even for a small AC intensity perturbation amplitude. Driving such a high current at high frequency resulted in significant attenuation and phase lag. To mitigate this effect, many systems used a reference photodiode which simultaneously measured the actual incident photon flux and applied this to the transfer function calculation. However, at very high frequencies, the large attenuation of the modulation intensity would still lead to large errors in this calculation. For this reason, we used separate LEDs to provide both the DC and AC illumination, with the response sampled by a lock-in amplifier. The custom-built experimental setup for IMPS/IMVS measurements is shown in Figure S1, Supporting Information. Hardware was controlled by custom-made LabVIEW software. A 5 mm extra High Brightness AlInGaP 626 nm LED (Broadcom) was driven directly from the sinusoidally modulated voltage output of an Agilent 33522B waveform generator (WFG). To provide an additional higher intensity DC offset, a larger red LED (Thorlabs M617L3) was driven by a Thorlabs LEDD1B driver (the LED driver was triggered via the Aux Out of the lock-in amplifier). All measurements were performed at ≈0.25 Suns equivalent intensity (based on the $J_{sc}$ of the devices). For IMPS measurements, the modulated photocurrent response of the cell under test was connected to the input of a lock-in amplifier (Stanford Research Systems SR865A), via a Femto DHPCA-100 transimpedance amplifier (TIA). For IMVS measurements, the cell was connected directly to the lock-in amplifier input (10 MΩ input impedance). The lock-in reference signal was provided from the WFG trigger connection. A silicon reference photodiode (Newport 818-UV) was used to calibrate the light intensity for calculation of the Q-plane IMPS response shown in Figure S6, Supporting Information.

The attenuation and phase shift of the modulated LED illumination at high frequency was measured using a high bandwidth, small area PIN photodiode (Hamamatsu S5971) via the TIA. Both the photodiode and TIA had bandwidths ≥100 MHz and so provided negligible impact on the measured attenuation and phase shift of the LED even at its highest modulation frequency (4 MHz). The desired LED modulated illumination amplitude was determined at low frequency (10 Hz). Typically IMPS/IMVS measurements were performed with a modulated amplitude of less than 10% of the DC intensity to ensure linearity of the cell response, while maintaining a good signal-to-noise ratio. We chose to limit the AC intensity amplitude to 5% of the DC offset to ensure linearity of the LED output and cell response, while still achieving a good signal-to-noise ratio. At each frequency, the amplitude of the modulated voltage signal from the WFG was increased until the amplitude of the LED illumination matched that predetermined value. The required AC voltage amplitude at each measurement frequency is shown in Figure S2, Supporting Information. The phase shift between the measured LED illumination and the applied voltage signal was also recorded at each frequency. Due to the high frequency modulation, and increased driving voltage required at these high frequencies to obtain a constant AC illumination amplitude, the phase shifts were significant. However, applying these measured phase shifts to the WFG reference output (this shifted the WFG trigger output signal phase relative to the output voltage signal) ensured that the lock-in amplifier was measuring in phase with the modulated light perturbation rather than the LED driving signal.

The modulated photocurrent/voltage response was recorded at individual frequencies over time after illumination, whereas the device $J_{sc}/V_{oc}$ was rising to a steady state, at a sampling interval of 0.5 s. Between each frequency condition, the device was left in the dark for long enough for an equilibrium condition to be reached. This procedure is shown schematically in Figure S3, Supporting Information.

*Measurements Performed using Commercial Electrochemical Workstation*: IMPS/IMVS and electrochemical impedance spectroscopy (EIS) measurements were performed on unmasked devices using a Zahner CIMPS-X photoelectrochemical workstation under 630 nm LED illumination. The LED intensity (DC and AC modulation) was set to match that used in the custom setup. For IMPS/IMVS, the measured frequency range was 1 MHz to 1 Hz. For EIS, the measured frequency range was 4 MHz to 1 Hz. All measurements using this system were performed after light soaking to achieve a steady state—i.e., 20 min light soaking for carbon devices.

*Transient Photocurrent/Photovoltage Measurements*: Measurements were performed using a 635 nm red laser diode driven by a WFG (Keysight 33522B), with a pulse length of 200 ns. Background illumination was provided by the same Thorlabs M617L3 LED, and at the same intensity, as used in IMPS/IMVS measurements.

Measurements were initiated once devices had equilibrated in the dark for up to tens of minutes. The LED bias light and laser diode were turned on using a fast metal-oxide-semiconductor field-effect transistor and optical shutter, respectively; both of which were controlled by the same trigger source. TPC/TPV traces were recorded at regular intervals (typically 0.7 s) by a Tektronix DPO3012 oscilloscope controlled by Tektronix SignalExpress software. For TPC, the device photocurrent was measured via Femto DHPCA-100 TIA. For TPV, the device under test was held at open-circuit by a custom-built voltage follower (1.5 TΩ input impedance).

## Supporting Information

Supporting Information is available from the Wiley Online Library or from the author.

## Conflict of Interest

The authors declare no conflict of interest.

## Data Availability Statement

The data that support the findings of this study are openly available in the Swansea University data archive at https://doi.org/10.5281/zenodo.4548274.

[1] Q. Jiang, Y. Zhao, X. Zhang, X. Yang, Y. Chen, Z. Chu, Q. Ye, X. Li, Z. Yin, J. You, *Nat. Photon.* **2019**, *13*, 460.

[2] I. L. Braly, D. W. deQuilettes, L. M. Pazos-Outón, S. Burke, M. E. Ziffer, D. S. Ginger, H. W. Hillhouse, *Nat. Photon.* **2018**, *12*, 355.

[3] Z. Liu, L. Krückemeier, B. Krogmeier, B. Klingebiel, J. A. Márquez, S. Levcenko, S. Öz, S. Mathur, U. Rau, T. Unold, T. Kirchartz, *ACS Energy Lett.* **2019**, *4*, 110.

[4] S. van Reenen, M. Kemerink, H. J. Snaith, *J. Phys. Chem. Lett.* **2015**, *6*, 3808.

[5] G. Richardson, S. E. J. O'Kane, R. G. Niemann, T. A. Peltola, J. M. Foster, P. J. Cameron, A. B. Walker, *Energy Environ. Sci.* **2016**, *9*, 1476.

[6] P. Calado, A. M. Telford, D. Bryant, X. Li, J. Nelson, B. C. O'Regan, P. R. F. Barnes, *Nat. Commun.* **2016**, *7*, 13831.

[7] A. Pockett, D. Raptis, S. M. P. Meroni, J. Baker, T. Watson, M. Carnie, *J. Phys. Chem. C* **2019**, *123*, 11414.

[8] F. Ebadi, M. Aryanpour, R. Mohammadpour, N. Taghavinia, *Sci. Rep.* **2019**, *9*, 11962.

[9] P. Calado, D. Burkitt, J. Yao, J. Troughton, T. M. Watson, M. J. Carnie, A. M. Telford, B. C. O'Regan, J. Nelson, P. R. F. Barnes, *Phys. Rev. Appl.* **2019**, *11*, 044005.

[10] B. C. O'Regan, P. R. F. Barnes, X. Li, C. Law, E. Palomares, J. M. Marin-Beloqui, *J. Am. Chem. Soc.* **2015**, *137*, 5087.

[11] A. Pockett, M. J. Carnie, *ACS Energy Lett.* **2017**, *2*, 1683.

[12] R. A. Belisle, W. H. Nguyen, A. R. Bowring, P. Calado, X. Li, S. J. C. Irvine, M. D. McGehee, P. R. F. Barnes, B. C. O'Regan, *Energy Environ. Sci.* **2017**, *10*, 192.

[13] A. Pockett, G. E. Eperon, T. Peltola, H. J. Snaith, A. Walker, L. M. Peter, P. J. Cameron, *J. Phys. Chem. C* **2015**, *119*, 3456.

[14] A. Pockett, G. E. Eperon, N. Sakai, H. J. Snaith, L. M. Peter, P. J. Cameron, *Phys. Chem. Chem. Phys.* **2017**, *19*, 5959.

[15] S. Ravishankar, C. Aranda, S. Sanchez, J. Bisquert, M. Saliba, G. Garcia-Belmonte, *J. Phys. Chem. C* **2019**, *123*, 6444.

[16] D. Klotz, G. Tumen-Ulzii, C. Qin, T. Matsushima, C. Adachi, *RSC Adv.* **2019**, *9*, 33436.

[17] T. S. Sherkar, C. Momblona, L. Gil-Escrig, J. Ávila, M. Sessolo, H. J. Bolink, L. J. A. Koster, *ACS Energy Lett.* **2017**, *2*, 1214.

[18] N. Li, S. Tao, Y. Chen, X. Niu, C. K. Onwudinanti, C. Hu, Z. Qiu, Z. Xu, G. Zheng, L. Wang, Y. Zhang, L. Li, H. Liu, Y. Lun, J. Hong, X. Wang, Y. Liu, H. Xie, Y. Gao, Y. Bai, S. Yang, G. Brocks, Q. Chen, H. Zhou, *Nat. Energy* **2019**, *4*, 408.

[19] J.-P. Correa-Baena, S.-H. Turren-Cruz, W. Tress, A. Hagfeldt, C. Aranda, L. Shooshtari, J. Bisquert, A. Guerrero, *ACS Energy Lett.* **2017**, *2*, 681.

[20] J. Jiménez-López, E. Palomares, *Nanoscale* **2019**, *11*, 20024.

[21] J. Bisquert, L. Bertoluzzi, I. Mora-Sero, G. Garcia-Belmonte, *J. Phys. Chem. C* **2014**, *118*, 18983.

[22] E. Ghahremanirad, A. Bou, S. Olyaee, J. Bisquert, *J. Phys. Chem. Lett.* **2017**, *8*, 1402.

[23] D. Moia, I. Gelmetti, P. Calado, W. Fisher, M. Stringer, O. Game, Y. Hu, P. Docampo, D. Lidzey, E. Palomares, J. Nelson, P. R. F. Barnes, *Energy Environ. Sci.* **2019**, *12*, 1296.

[24] S. Ravishankar, A. Riquelme, S. K. Sarkar, M. Garcia-Batlle, G. Garcia-Belmonte, J. Bisquert, *J. Phys. Chem. C* **2019**, *123*, 24995.

[25] A. Bou, A. Pockett, D. Raptis, T. Watson, M. J. Carnie, J. Bisquert, *J. Phys. Chem. Lett.* **2020**, *11*, 8654.

[26] E. Guillén, F. J. Ramos, J. A. Anta, S. Ahmad, *J. Phys. Chem. C* **2014**, *118*, 22913.

[27] A. Albadri, P. Yadav, M. Alotaibi, N. Arora, A. Alyamani, H. Albrithen, M. I. Dar, S. M. Zakeeruddin, M. Grätzel, *J. Phys. Chem. C* **2017**, *121*, 24903.

[28] A. Riquelme, F. E. Gálvez, L. Contreras-Bernal, H. Míguez, J. A. Anta, *J. Appl. Phys.* **2020**, *12*, 133103.

[29] E. A. Ponomarev, L. M. Peter, *J. Electroanal. Chem.* **1995**, *396*, 219.

[30] O. Almora, Y. Zhao, X. Du, T. Heumueller, G. J. Matt, G. Garcia-Belmonte, C. J. Brabec, *Nano Energy* **2020**, *75*, 104982.

[31] S. Ravishankar, C. Aranda, P. P. Boix, J. A. Anta, J. Bisquert, G. Garcia-Belmonte, *J. Phys. Chem. Lett.* **2018**, *9*, 3099.

[32] L. M. Peter, E. A. Ponomarev, G. Franco, N. J. Shaw, *Electrochim. Acta* **1999**, *45*, 549.

[33] H.-S. Kim, I.-H. Jang, N. Ahn, M. Choi, A. Guerrero, J. Bisquert, N.-G. Park, *J. Phys. Chem. Lett.* **2015**, *6*, 4633.

[34] M. F. Aygüler, A. G. Hufnagel, P. Rieder, M. Wussler, W. Jaegermann, T. Bein, V. Dyakonov, M. L. Petrus, A. Baumann, P. Docampo, *ACS Appl. Mater. Interfaces* **2018**, *10*, 11414.

[35] M. Li, C. Zhao, Z.-K. Wang, C.-C. Zhang, H. K. H. Lee, A. Pockett, J. Barbé, W. C. Tsoi, Y.-G. Yang, M. J. Carnie, X.-Y. Gao, W.-X. Yang, J. R. Durrant, L.-S. Liao, S. M. Jain, *Adv. Energy Mater.* **2018**, *8*, 1801509.